

A global inversion-symmetry-broken phase inside the pseudogap region of $\text{YBa}_2\text{Cu}_3\text{O}_y$

L. Zhao^{1,2}, C. A. Belvin³, R. Liang^{4,5}, D. A. Bonn^{4,5}, W. N. Hardy^{4,5}, N. P. Armitage⁶
& D. Hsieh^{1,2}

¹*Department of Physics, California Institute of Technology, Pasadena, CA 91125, USA.*

²*Institute for Quantum Information and Matter, California Institute of Technology, Pasadena, CA 91125, USA.*

³*Wellesley College, Wellesley, MA 02481, USA.*

⁴*Department of Physics and Astronomy, University of British Columbia, Vancouver, British Columbia V6T 1Z1, Canada.*

⁵*Canadian Institute for Advanced Research, Toronto, Ontario M5G 1Z8, Canada.*

⁶*Institute of Quantum Matter, Department of Physics and Astronomy, The Johns Hopkins University, Baltimore, Maryland 21218, USA.*

The phase diagram of cuprate high-temperature superconductors features an enigmatic pseudogap region that is characterized by a partial suppression of low energy electronic excitations¹. Polarized neutron diffraction²⁻⁴, Nernst effect⁵, THz polarimetry⁶ and ultrasound measurements⁷ on $\text{YBa}_2\text{Cu}_3\text{O}_y$ suggest that the pseudogap onset below a temperature T^* coincides with a bona fide thermodynamic phase transition that breaks time-reversal, four-fold rotation and mirror symmetries respectively. However, the full point group above and below T^* has not been resolved and the fate of this transition as T^* approaches the superconducting critical temperature T_c is poorly understood. Here we reveal the point group of $\text{YBa}_2\text{Cu}_3\text{O}_y$ inside its pseudogap and neighboring regions using high sensitivity linear and second harmonic optical anisotropy measurements. We show that spatial inversion and two-fold rotational symmetries are broken below T^* while mirror symmetries perpendicular to the Cu-O plane are absent at all temperatures. This transition occurs over a wide doping range and persists inside the superconducting dome, with no detectable coupling to either charge ordering or superconductivity. These results suggest that the pseudogap region coincides with an odd-parity order that does not arise from a competing Fermi surface instability and exhibits a quantum phase transition inside the superconducting dome.

The crystal system and point group of a material are encoded in the structure of its second- and higher-rank optical susceptibility tensors⁸, which can be determined from the anisotropy of its linear and nonlinear optical responses. The second harmonic (SH) response is particularly sensitive to the presence of global inversion symmetry because unlike the linear electric-dipole susceptibility tensor χ_{ij}^{ED} , which is allowed in all crystal systems, the SH electric-dipole susceptibility tensor χ_{ijk}^{ED} vanishes in centrosymmetric point groups, leaving typically the far weaker electric-quadrupole term χ_{ijkl}^{EQ} as the primary bulk radiation source^{9,10}. For these reasons, it has been proposed that optical SH generation may be an effective probe of inversion symmetry breaking in the cuprates¹¹.

To fully resolve the spatial symmetries underlying the pseudogap and its neighboring regions, we performed both linear and SH optical rotational anisotropy (RA) measurements on de-twinned single crystals of $\text{YBa}_2\text{Cu}_3\text{O}_y$ as a function of oxygen content and temperature. The RA measurements track variations in the intensities of light reflected at the fundamental (I^ω) and SH frequencies ($I^{2\omega}$) of an obliquely incident laser beam, which is resonant with the O $2p$ to Cu $3d$ charge transfer energy ($\hbar\omega = 1.5$ eV), as the scattering plane is rotated about the c -axis (Fig. 1a). The use of a recently developed rotating optical grating based technique¹² made it possible to perform full 360° sweeps of the scattering plane angle (φ) over large temperature ranges while keeping the incident beam spot (~ 100 μm) fixed to the same location on the crystal to within a few microns.

We first simulate the RA patterns expected from hole doped $\text{YBa}_2\text{Cu}_3\text{O}_y$ ($y > 6$) based on its reported orthorhombic mmm crystallographic point group¹³, which is inversion symmetric and consists of three generators m_{ac} , m_{bc} and m_{ab} that denote mirror symmetries across the ac , bc and ab planes. Unlike its tetragonal parent ($y = 6$) compound¹⁴, the point group of hole doped $\text{YBa}_2\text{Cu}_3\text{O}_y$ only endows the crystal with two-fold (C_2) rather than four-fold (C_4) rotational symmetry about the c -axis because the excess oxygen atoms form chains that run along the b axis (Fig. 1a). Figure 1b shows representative linear and SH RA patterns computed in the electric-dipole $I^\omega(\varphi) \propto |\hat{e}_i^\omega(\varphi)\chi_{ij}^{ED}\hat{e}_{j,0}^\omega(\varphi)|^2 I_0$ and electric-quadrupole $I^{2\omega}(\varphi) \propto |\hat{e}_i^{2\omega}(\varphi)\chi_{ijkl}^{EQ}\hat{e}_{j,0}^\omega(\varphi)\partial_k\hat{e}_{l,0}^\omega(\varphi)|^2 I_0^2$ approximations respectively, where I_0 is the incident beam intensity and both the incident (in) and reflected (out) polarizations \hat{e}_0 and \hat{e} are selected to be perpendicular ($S_{\text{in}}-S_{\text{out}}$) to the scattering plane (see Supplementary Section S1 for other polarization geometries). The orthorhombic crystal system is identifiable by an ovular $I^\omega(\varphi)$ pattern with maxima and minima aligned strictly along the a and b axes¹⁵ while the mmm point group is identifiable by a four-lobed $I^{2\omega}(\varphi)$ pattern that is mirror symmetric about the a and b axes.

Figure 2 shows linear and SH RA data from $\text{YBa}_2\text{Cu}_3\text{O}_y$ with hole-doping levels (p) of 0.125 ($y = 6.67$; underdoped; $T_c = 65$ K), 0.135 ($y = 6.75$; underdoped; $T_c = 75$ K), 0.165 ($y = 6.83$; overdoped; $T_c = 90$ K), and 0.195 ($y = 6.92$; overdoped; $T_c = 95$ K).

= 6.92; optimal doped; $T_c = 92$ K) and 0.190 ($y = 7.0$; overdoped; $T_c = 86$ K) measured at room temperature ($T > T^*$) in S_{in} - S_{out} geometry (see Supplementary Section S2 for all other geometries). In the linear RA data, we see that the anisotropy ($\chi_{xx}^{ED} - \chi_{yy}^{ED}$) becomes more pronounced with hole doping as expected due to the filling of Cu-O chains. However, in contrast to Fig. 1b, the intensity maxima and minima are rotated away from the a and b axes, indicating an absence of m_{ac} and m_{bc} symmetries consistent with a monoclinic distortion. In fact, by using the structure of χ_{ij}^{ED} for a monoclinic crystal system in the expression for $I^\omega(\varphi)$, excellent fits to the data are obtained (Fig. 2). In the SH RA data, we also find clear violations of the mmm point group symmetries at all doping levels. In particular, the alternation in lobe magnitude as a function of φ and the rotation of the lobe bisectors away from the a and b axes indicate an absence of m_{ac} and m_{bc} symmetries consistent with the linear RA data. We find excellent agreement of the data with an electric-quadrupole induced SH response from the centrosymmetric $2/m$ monoclinic point group (Fig. 2), which consists of two generators 2 and m that denote C_2 and m_{ab} symmetries. On the contrary, fits to electric-dipole induced SH from the non-centrosymmetric 2 and m monoclinic point groups, as well as to magnetic-dipole-induced¹¹ or surface electric-dipole-induced SH from the $2/m$ point group, do not adequately describe the data (see Supplementary Section S3).

The degree of monoclinicity, which can be qualitatively tracked via the angular deviation of the intensity maximum (lobe bisector) in the linear (SH) RA data away from the a -axis, decreases monotonically between $y = 6.67$ and $y = 7$ as shown in Fig. 2. This suggests that the absence of m_{ac} and m_{bc} symmetries at all measured temperatures above T^* (see Supplementary Section S4) originates from vacancy induced monoclinic distortions of the oxygen sublattice, which are also known to be present in $La_{2-x}Sr_xCuO_4$ ¹⁶. This interpretation is further supported by recent SH RA measurements performed near the charge transfer resonance of layered perovskite iridates^{9,10}, which revealed subtle oxygen sublattice distortions that are difficult to resolve using diffraction based probes.

Having established the point group of hole-doped $\text{YBa}_2\text{Cu}_3\text{O}_y$ above T^* , we proceed to search for changes in symmetry across the strange metal to pseudogap boundary. Previous infrared conductivity experiments¹⁷ have shown that optical transition rates at frequencies well above the pseudogap energy scale ($\hbar\omega \gtrsim 0.3$ eV) do not exhibit any measurable temperature dependence across T^* . As a corollary, any temperature dependent change in magnitude of χ_{ij}^{ED} or χ_{ijkl}^{EQ} at the frequencies used in this study ($\hbar\omega = 1.5$ eV and $2\hbar\omega = 3$ eV) should be correspondingly weak. Figures 3a-d show the temperature dependences of both the linear and SH intensities measured at a fixed value of φ in $S_{\text{in}}-S_{\text{out}}$ geometry. For all four doping levels studied in Fig. 2, we observe no change in the linear response as a function of temperature as expected. Surprisingly however, all of the SH responses exhibit a significant order-parameter-like upturn below a doping dependent critical temperature T_Ω . This dichotomy between the linear and SH responses can naturally be reconciled if bulk inversion symmetry is broken below T_Ω , which would turn on a new and stronger source of electric-dipole induced SH radiation on top of the already existing electric-quadrupole contribution.

By plotting the doping dependence of T_Ω atop the phase diagram of $\text{YBa}_2\text{Cu}_3\text{O}_y$ (Fig. 3e), we find that the observed onset of inversion symmetry breaking coincides very well with the pseudogap phase boundary T^* defined by spin-polarized neutron diffraction²⁻⁴, Nernst anisotropy⁵, THz polarimetry⁶ and resonant ultrasound⁷ measurements in the optimal and underdoped regions, suggesting a common underlying mechanism. Moreover, we detect an onset of inversion symmetry breaking even inside the superconducting dome in the overdoped region, which may imply a quantum phase transition slightly beyond $p = 0.20$ near where the pseudogap energy scale has also been extrapolated to vanish¹⁸. Interestingly, the temperature dependence of the SH intensity shows no measurable anomalies upon crossing either the superconducting or the charge density wave ordering^{19,20} temperatures (Fig. 3e) and does not rapidly diminish at lower temperatures like the Nernst anisotropy⁵, which may be caused by charge density wave ordering²¹. This shows that unlike the superconducting and charge ordered phases, which are competing Fermi surface instabilities²², the observed inversion symmetry broken phase is independent of and coexistent with both of them.

To determine which symmetries in addition to inversion are removed from the $2/m$ point group below the pseudogap temperature, we performed a comparative study of the SH RA data measured above and below T_Ω . Figure 4a shows RA patterns measured at 295 K and 30 K in $S_{\text{in}}-S_{\text{out}}$ geometry for the optimal doped sample ($T_\Omega \sim 110$ K), which is representative of all other doping levels studied (see Supplementary Section S5). Below T_Ω we see that the SH intensity is enhanced in a φ dependent manner that preserves the two-fold rotational symmetry of the pattern, which ostensibly implies that C_2 is preserved in the crystal. However this interpretation can be ruled out because the inferred above electric-dipole induced SH radiation is strictly forbidden by symmetry in $S_{\text{in}}-S_{\text{out}}$ geometry for any point group (non-magnetic or magnetic) that contains C_2 (see Supplementary Section S3). The only alternative interpretation is that the order parameter below T_Ω breaks C_2 symmetry, but is obscured in the RA patterns because of spatial averaging over domains of two degenerate orientations of the order parameter that are related by 180° rotation about the c -axis. This would imply a characteristic domain length scale that is much smaller than our laser spot size and consistently explains the absence of any signatures of C_2 breaking below T^* in Nernst effect⁵ and THz polarimetry⁶ data as well as the need for multiple magnetic domains to refine the polarized neutron diffraction data^{2-4,23}, which are all integrated over even larger areas of the crystal compared to our measurements.

The set of all non-centrosymmetric subgroups of $2/m$ that do not contain C_2 consists of the two independent magnetic point groups $2'/m$ and $m1'$ and their associated magnetic and non-magnetic subgroups (see Supplementary Section S6), where the generators $2'$, m and $1'$ denote C_2 combined with time-reversal, m_{ab} and the identity operation combined with time-reversal respectively. Using the two-domain ($\alpha = 1, 2$) averaged expression $I^{2\omega}(\varphi) \propto \sum_{\alpha=1,2} |\hat{e}_i^{2\omega}(\varphi) \chi_{ijkl}^{EQ} \hat{e}_{j,0}^\omega(\varphi) \partial_k \hat{e}_{l,0}^\omega(\varphi) + \hat{e}_i^{2\omega}(\varphi) \chi_{ijk,\alpha}^{ED} \hat{e}_{j,0}^\omega(\varphi) \hat{e}_{k,0}^\omega(\varphi)|^2 I_0^2$, we were able to reproduce all features of the low temperature SH RA data, including the small peaks around the b -axis (Fig. 4a), by applying the structure of $\chi_{ijk,\alpha}^{ED}$ for either the $2'/m$ or $m1'$ point group. The decomposition of the fit into its two single domain components is shown in Fig. 4b to explicitly illustrate the loss of C_2 . An equally good fit to the data can naturally be achieved

using any magnetic or non-magnetic subgroup of $2'/m$ or $m1'$ because they necessarily allow the same or more non-zero independent $\chi_{ijk,\alpha}^{ED}$ tensor elements. Therefore, while further removal of symmetry elements from $2'/m$ or $m1'$ is not necessary to explain the low temperature data, it cannot be completely ruled out.

In conclusion, our results show that the pseudogap region in $\text{YBa}_2\text{Cu}_3\text{O}_y$ is bounded by a line of phase transitions associated with the loss of global inversion and C_2 symmetries. Although previous THz polarimetry measurements on hole-doped $\text{YBa}_2\text{Cu}_3\text{O}_y$ thin films reported the onset of a linear dichroic response near T^* that breaks m_{ac} and m_{bc} symmetries⁶, we find that these symmetries are already broken in the crystallographic structure above T^* and are thus necessarily absent in any tensor response that turns on below T^* . The low symmetry of the point group (likely $2'/m$ or $m1'$) underlying the pseudogap region cannot be explained by stripe²⁴ or nematic⁵ type orders alone, which have also been reported to develop below T^* . Instead it suggests the presence of an odd-parity magnetic order parameter, which is consistent with theoretical proposals involving a ferroic ordering of current loops circulating within the Cu-O octahedra^{11,25-27}, local Cu-site magnetic-quadrupoles²⁸, O-site moments²⁹ or magneto-electric multipoles generated dynamically through spin-phonon coupling³⁰. Regardless of microscopic origin, our results suggest that this order undergoes a quantum phase transition inside the superconducting dome slightly beyond optimal doping, which may be responsible for the enhanced T_c and quasiparticle mass³¹ observed in its vicinity. Interestingly, a similar odd-parity magnetic phase has also recently been found in the pseudogap region of a $5d$ transition metal analogue of the cuprates³², which hints at a possibly more robust connection between the pseudogap and this unusual form of broken symmetry.

Acknowledgements

We thank D. N. Basov, P. Bourges, B. Keimer, S. A. Kivelson, P. A. Lee, J. W. Lynn, J. Orenstein, S. Raghu, B. Ramshaw, C. Varma and N.-C. Yeh for valuable discussions. This work was supported by ARO Grant W911NF-13-1-0059. Instrumentation for the RA measurements was partially supported by ARO DURIP Award W911NF-13-1-0293. D.H. acknowledges funding provided by the Institute for Quantum Information and Matter, an NSF Physics Frontiers Center (PHY-1125565) with support of the Gordon and Betty Moore Foundation through Grant GBMF1250. N.P.A. acknowledges support from ARO Grant W911NF-15-1-0560. Work at the University of British Columbia was supported by the Canadian Institute for Advanced Research and the Natural Science and Engineering Research Council.

Author contributions

L.Z., D.H. and N.P.A. planned the experiment. L.Z. and C.A.B. performed the RA measurements and N.P.A. determined the crystal alignment. L.Z., D.H. and N.P.A. analysed the data. R.L., D.A.B. and W.N.H. prepared and characterized the samples. L.Z. and D.H. wrote the manuscript.

Additional information

Supplementary information accompanies this paper. Correspondence and requests for materials should be addressed to D.H. (dhsieh@caltech.edu).

References

1. Keimer, B., Kivelson, S. A., Norman, M. R., Uchida, S. & Zaanen, J. From quantum matter to high-temperature superconductivity in copper oxides. *Nature* **518**, 179–186 (2015).
2. Fauqué, B. *et al.* Magnetic order in the pseudogap phase of high- T_c superconductors. *Phys. Rev. Lett.* **96**, 197001 (2006).
3. Mook, H. A., Sidis, Y., Fauqué, B., Balédent, V. & Bourges, P. Observation of magnetic order in a superconducting $\text{YBa}_2\text{Cu}_3\text{O}_{6.6}$ single crystal using polarized neutron scattering. *Phys. Rev. B* **78**, 20506 (2008).
4. Mangin-Thro, L., Sidis, Y., Wildes, A. & Bourges, P. Intra-unit-cell magnetic correlations near optimal doping in $\text{YBa}_2\text{Cu}_3\text{O}_{6.85}$. *Nat. Commun.* **6**, 7705 (2015).
5. Daou, R. *et al.* Broken rotational symmetry in the pseudogap phase of a high- T_c superconductor. *Nature* **463**, 519–522 (2010).
6. Lubashevsky, Y., Pan, L., Kirzhner, T., Koren, G. & Armitage, N. P. Optical birefringence and dichroism of cuprate superconductors in the THz regime. *Phys. Rev. Lett.* **112**, 147001 (2014).
7. Shekhter, A. *et al.* Bounding the pseudogap with a line of phase transitions in $\text{YBa}_2\text{Cu}_3\text{O}_{6+\delta}$. *Nature* **498**, 75–77 (2013).
8. Boyd, R. W. *Nonlinear Optics*. (Academic Press, 2003).
9. Torchinsky, D. H. *et al.* Structural distortion-induced magnetoelastic locking in Sr_2IrO_4 revealed through nonlinear optical harmonic generation. *Phys. Rev. Lett.* **114**, 96404 (2015).
10. Hogan, T. *et al.* Structural investigation of the bilayer iridate $\text{Sr}_3\text{Ir}_2\text{O}_7$. *Phys. Rev. B* **93**, 134110 (2016).

11. Simon, M. E. & Varma, C. M. Symmetry considerations for the detection of second-harmonic generation in cuprates in the pseudogap phase. *Phys. Rev. B* **67**, 54511 (2003).
12. Torchinsky, D. H., Chu, H., Qi, T., Cao, G. & Hsieh, D. A low temperature nonlinear optical rotational anisotropy spectrometer for the determination of crystallographic and electronic symmetries. *Rev. Sci. Instrum.* **85**, 83102 (2014).
13. Shaked, H. *Crystal structures of the high-T_c superconducting copper-oxides*. (Elsevier Science Publishers B.V., 1994).
14. Jorgensen, J. D. *et al.* Structural properties of oxygen-deficient YBa₂Cu₃O_{7-δ}. *Phys. Rev. B* **41**, 1863–1877 (1990).
15. Schmid, H. *et al.* Polarized light and X-ray precession study of the ferroelastic domains of YBa₂Cu₃O_{7-δ}. *Z. Für Phys. B Condens. Matter* **72**, 305–322 (1988).
16. Reehuis, M. *et al.* Crystal structure and high-field magnetism of La₂CuO₄. *Phys. Rev. B* **73**, 144513 (2006).
17. Lee, Y. S. *et al.* Electrodynamics of the nodal metal state in weakly doped high-T_c cuprates. *Phys. Rev. B* **72**, 54529 (2005).
18. Tallon, J. L. & Loram, J. W. The doping dependence of T* – what is the real high-T_c phase diagram? *Phys. C Supercond.* **349**, 53–68 (2001).
19. Blanco-Canosa, S. *et al.* Resonant x-ray scattering study of charge-density wave correlations in YBa₂Cu₃O_{6+x}. *Phys. Rev. B* **90**, 54513 (2014).
20. Hücker, M. *et al.* Competing charge, spin, and superconducting orders in underdoped YBa₂Cu₃O_y. *Phys. Rev. B* **90**, 54514 (2014).
21. Cyr-Choinière, O. *et al.* Two types of nematicity in the phase diagram of the cuprate superconductor YBa₂Cu₃O_y. *Phys. Rev. B* **92**, 224502 (2015).
22. Chang, J. *et al.* Direct observation of competition between superconductivity and charge density wave order in YBa₂Cu₃O_{6.67}. *Nat. Phys.* **8**, 871–876 (2012).

23. Li, Y. *et al.* Unusual magnetic order in the pseudogap region of the superconductor $\text{HgBa}_2\text{CuO}_{4+\delta}$. *Nature* **455**, 372–375 (2008).
24. Parker, C. V. *et al.* Fluctuating stripes at the onset of the pseudogap in the high- T_c superconductor $\text{Bi}_2\text{Sr}_2\text{CaCu}_2\text{O}_{8+x}$. *Nature* **468**, 677–680 (2010).
25. Varma, C. M. Non-Fermi-liquid states and pairing instability of a general model of copper oxide metals. *Phys. Rev. B* **55**, 14554–14580 (1997).
26. Simon, M. E. & Varma, C. M. Detection and implications of a time-reversal breaking state in underdoped cuprates. *Phys. Rev. Lett.* **89**, 247003 (2002).
27. Yakovenko, V. M. Tilted loop currents in cuprate superconductors. *Phys. B Condens. Matter* **460**, 159–164 (2015).
28. Lovesey, S. W., Khalyavin, D. D. & Staub, U. Ferro-type order of magneto-electric quadrupoles as an order-parameter for the pseudo-gap phase of a cuprate superconductor. *J. Phys. Condens. Matter* **27**, 292201 (2015).
29. Moskvina, A. S. Pseudogap phase in cuprates: Oxygen orbital moments instead of circulating currents. *JETP Lett.* **96**, 385–390 (2013).
30. Fechner, M., Fierz, M. J. A., Thöle, F., Staub, U. & Spaldin, N. A. Quasistatic magnetoelectric multipoles as order parameter for pseudogap phase in cuprate superconductors. *Phys. Rev. B* **93**, 174419 (2016).
31. Ramshaw, B. J. *et al.* Quasiparticle mass enhancement approaching optimal doping in a high- T_c superconductor. *Science* **348**, 317–320 (2015).
32. Zhao, L. *et al.* Evidence of an odd-parity hidden order in a spin-orbit coupled correlated iridate. *Nat. Phys.* **12**, 32–36 (2016).
33. Xia, J. *et al.* Polar Kerr-effect measurements of the high-temperature $\text{YBa}_2\text{Cu}_3\text{O}_{6+x}$ superconductor: Evidence for broken symmetry near the pseudogap temperature. *Phys. Rev. Lett.* **100**, 127002 (2008).

Figure 1

Layout of optical anisotropy experiment and predicted response of $\text{YBa}_2\text{Cu}_3\text{O}_y$.

a, The intensity of light reflected at the fundamental (I^ω) and SH ($I^{2\omega}$) frequencies of an obliquely incident beam is measured as a function of the angle (φ) between the scattering plane and the a - c plane of $\text{YBa}_2\text{Cu}_3\text{O}_y$. The Cu-O chains run along the b axis. The incident photon energy (1.5 eV) is resonant with the O $2p$ to Cu $3d$ charge transfer transition (inset). The polarization of the incident (in) and reflected (out) beams can be selected to lie either parallel (P) or perpendicular (S) to the scattering plane. **b**, Rotational anisotropy of the electric-dipole induced linear response and electric-quadrupole induced SH response simulated for the orthorhombic crystal system and the mmm point group respectively in $S_{\text{in}}-S_{\text{out}}$ geometry. The crystallographic a and b axes are aligned respectively along the laboratory x and y axes.

Figure 2

Crystal system and point group of $\text{YBa}_2\text{Cu}_3\text{O}_y$ above T^* . Polar plots of $I^\omega(\varphi)$ and $I^{2\omega}(\varphi)$ measured at $T = 295$ K in $S_{\text{in}}-S_{\text{out}}$ geometry from $\text{YBa}_2\text{Cu}_3\text{O}_y$ with **a**, $y = 6.67$, **b**, 6.75, **c**, 6.92 and **d**, 7.0. The $I^\omega(\varphi)$ and $I^{2\omega}(\varphi)$ data sets, which have intensity error bars of approximately $\pm 1\%$ and $\pm 10\%$ respectively, are each plotted on the same intensity scale with a scaling ratio of $I^\omega(\varphi):I^{2\omega}(\varphi) \approx 1:3 \times 10^{-11}$. The former are fit to the electric-dipole induced linear response of the monoclinic crystal system (red lines) and the latter are fit to the electric-quadrupole induced SH response of the $2/m$ point group (blue lines). The angular deviations of the maxima of $I^\omega(\varphi)$ and lobe bisectors of $I^{2\omega}(\varphi)$ away from the a axis are shaded red and blue respectively for clarity.

Figure 3

Inversion symmetry breaking transition across the phase diagram of $\text{YBa}_2\text{Cu}_3\text{O}_y$.

Temperature dependence of the linear and SH response of $\text{YBa}_2\text{Cu}_3\text{O}_y$ with **a**, $y = 6.67$, **b**, 6.75, **c**, 6.92 and **d**, 7.0 normalized to their room temperature values. Data were taken in $S_{\text{in}}-S_{\text{out}}$ geometry at angles φ corresponding to the smaller SH lobe maxima at $T = 295$ K (see Fig. 2). The error bars represent the standard deviation of the intensity over 60 independent measurements. Blue curves overlaid on the data are guides to the eye. The inversion symmetry breaking transition temperatures T_Ω determined from the SH response are marked by the dashed lines. The width of the shaded gray intervals represent the uncertainty in T_Ω . **e**, Temperature versus doping phase diagram of $\text{YBa}_2\text{Cu}_3\text{O}_y$. The values of T_Ω (red circles) coincide with the onset of the pseudogap as defined by spin-polarized neutron diffraction²⁻⁴ (blue squares), Nernst effect⁵ (open blue squares), THz polarimetry⁶ (purple diamonds) and resonant ultrasound⁷ (orange circles). The onset of a polar Kerr effect³³ (green diamonds) and short-range charge order as determined by x-ray diffraction^{19,20} (green squares) occur at temperatures below T^* . Error bars denote the uncertainty in the onset temperatures. The superconducting transition temperatures of the samples used in our work are denoted by gray circles.

Figure 4

Point group symmetry of YBa₂Cu₃O_y below T*. **a**, Polar plot of $I^{2\omega}(\varphi)$ measured at $T = 30$ K in S_{in}–S_{out} geometry from YBa₂Cu₃O_{6.92} (squares). The intensity error bars are approximately $\pm 10\%$. The blue curve is a best fit to the average of two 180° rotated domains with 2'/m point group symmetry as described in the text. The fit to the $T = 295$ K data (pink shaded area) reproduced from Fig. 2c is overlaid for comparison. **b**, Decomposition of the fit to the $T = 30$ K data (shaded blue area) into its individual domain contributions (shaded orange and purple areas).

Methods

Material growth. YBa₂Cu₃O_y single crystals were grown in non-reactive BaZrO₃ crucibles using a self-flux technique. The CuO-chain oxygen content was set to $y = 6.67, 6.75, 6.92$ and 7.0 by annealing in a flowing O₂:N₂ mixture and homogenized by further annealing in a sealed quartz ampoule, together with ceramic at the same oxygen content. The absolute oxygen content (y) is accurate to ± 0.01 based on iodometric titration. The crystals used in our experiments were de-twinned and aligned to high accuracy by x-ray Laue diffraction.

Optical RA measurements. The RA measurements were performed using a rotating optical grating based technique¹² with ultrashort (~80 fs) optical pulses produced from a regeneratively amplified Ti:sapphire laser operating at a 10 kHz repetition rate. The angle of incidence was $\sim 30^\circ$ and the incident fluence was maintained below 1 mJ cm^{-2} to ensure no laser-induced changes to the samples (see Supplementary Section S7). Alignment of the optical axis to the crystallographic c -axis was determined to better than 0.1° accuracy as described in Supplementary Section S8. Reflected fundamental ($\lambda = 800 \text{ nm}$) and SH light ($\lambda = 400 \text{ nm}$) were collected using photodiodes and photomultiplier tubes respectively. Crystals were sealed in a dry environment during transportation and immediately pumped down to pressures $< 5 \times 10^{-6}$ torr for measurements.

Fitting procedure. The high-temperature ($T > T_\Omega$) linear optical anisotropy data were fitted to the expression $I^\omega(\varphi) = A |\hat{e}_i^\omega(\varphi) \chi_{ij}^{ED} \hat{e}_{j,0}^\omega(\varphi)|^2 I_0$ and the high- ($T > T_\Omega$) and low-temperature ($T < T_\Omega$) SH anisotropy data were fitted to the expressions $I^{2\omega}(\varphi) = |A \hat{e}_i^{2\omega}(\varphi) \chi_{ijkl}^{EQ} \hat{e}_{j,0}^\omega(\varphi) \partial_k \hat{e}_{l,0}^\omega(\varphi)|^2 I_0^2$ and $I^{2\omega}(\varphi) = (|A|^2 / 2) \sum_{\alpha=1,2} |\hat{e}_i^{2\omega}(\varphi) \chi_{ijkl}^{EQ} \hat{e}_{j,0}^\omega(\varphi) \partial_k \hat{e}_{l,0}^\omega(\varphi) + \hat{e}_i^{2\omega}(\varphi) \chi_{ijk,\alpha}^{ED} \hat{e}_{j,0}^\omega(\varphi) \hat{e}_{k,0}^\omega(\varphi)|^2 I_0^2$ respectively. Here A is a constant determined by the experimental geometry, \hat{e}_0 and \hat{e} are the polarizations of the incoming and outgoing light in

the frame of the crystal, χ_{ij}^{ED} is the linear electric-dipole susceptibility tensor, χ_{ijkl}^{EQ} is the SH electric-quadrupole susceptibility tensor and $\chi_{ijk,\alpha}^{ED}$ is the SH electric-dipole susceptibility tensor. The $\alpha = 1$ and $\alpha = 2$ versions of the latter are related by 180° rotation about the c -axis. The non-zero independent elements of these tensors in the frame of the crystal are determined by applying the monoclinic crystal symmetries to χ_{ij}^{ED} and the appropriate point group symmetries ($2/m$ for χ_{ijkl}^{EQ} and either $2'/m$ or $m1'$ for $\chi_{ijk,\alpha}^{ED}$) and degenerate SH permutation symmetries to χ_{ijkl}^{EQ} and $\chi_{ijk,\alpha}^{ED}$. These operations reduce χ_{ij}^{ED} to 5 non-zero independent elements (xx, xz, yy, zx, zz), χ_{ijkl}^{EQ} to 28 non-zero independent elements ($xxxx, yyyy, zzzz, xxyy = xyxx, yyxx = yxxy, xyxy, yxyx, xxzz = xzzx, zzzx = zxxz, xzxz, zxxz, yyzz = yzzz, zzyy = zyzy, yzyz, zyzzy, xzyy = xyyz, xyyz, yxzy = yyzx, yxyz = yzyx, yyxz = yzxy, zxyy = zyxx, zyxy, zxxx, xxzx, xxxz = xzxx, xzzz, zzzz, zzzx = zxzz$), and $\chi_{ijk,\alpha}^{ED}$ to 10 non-zero independent elements ($xxx, xyx = xxy, xyy, xzz, yxx, yyx = yxy, yyy, yzz, zzx = zxz, zzy = zyz$). Values of $R^2 > 0.95$ were achieved for all fits shown. However the fitted values of the susceptibility tensor elements are not unique. Therefore the fits serve only to address the qualitative question of whether a certain point group can or cannot reproduce the data. They are not intended to convey any quantitative information about the magnitudes of various tensor elements.

Data availability. The data that support the plots within this paper and other findings of this study are available from the corresponding author upon reasonable request.

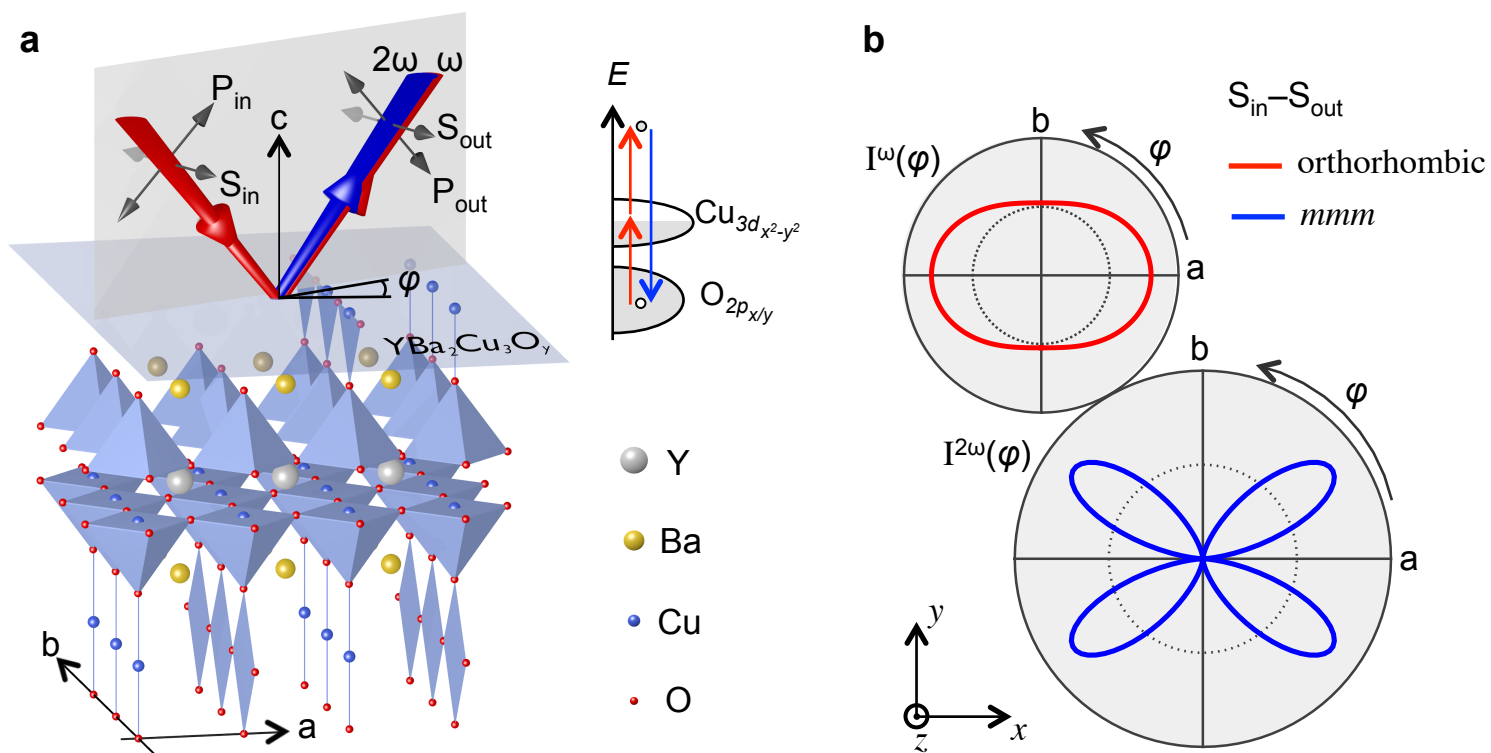


Fig. 1

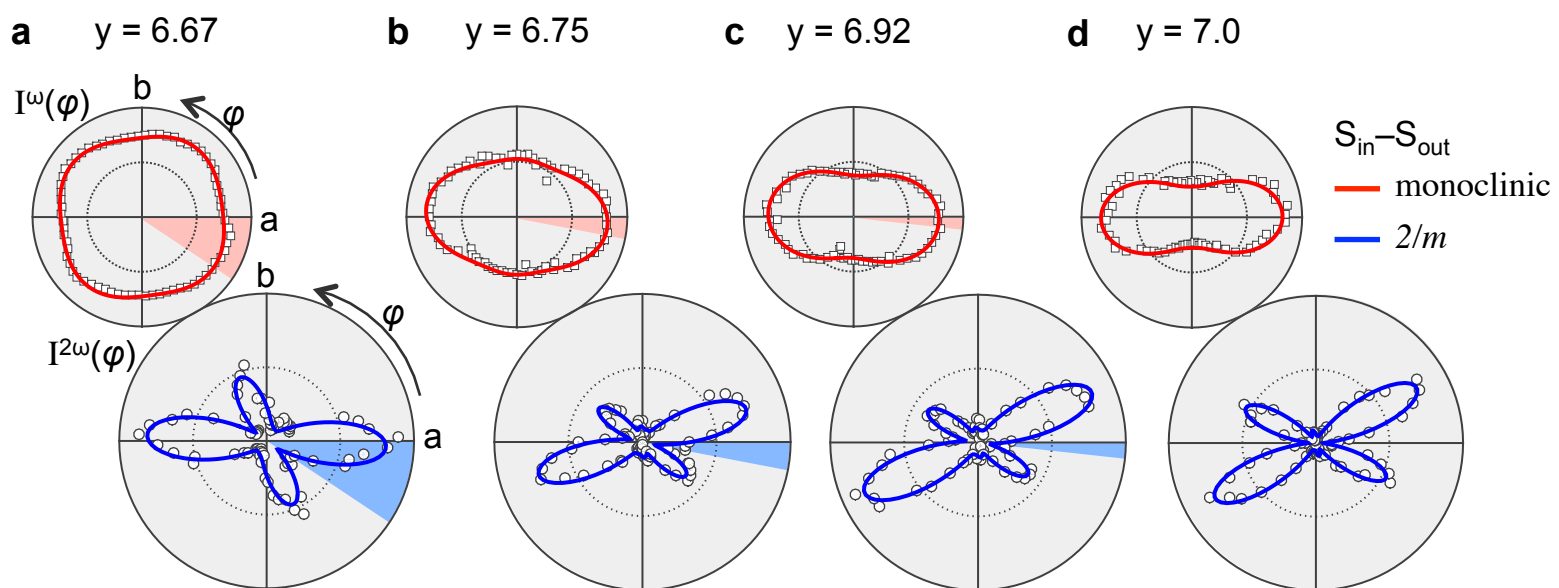


Fig. 2

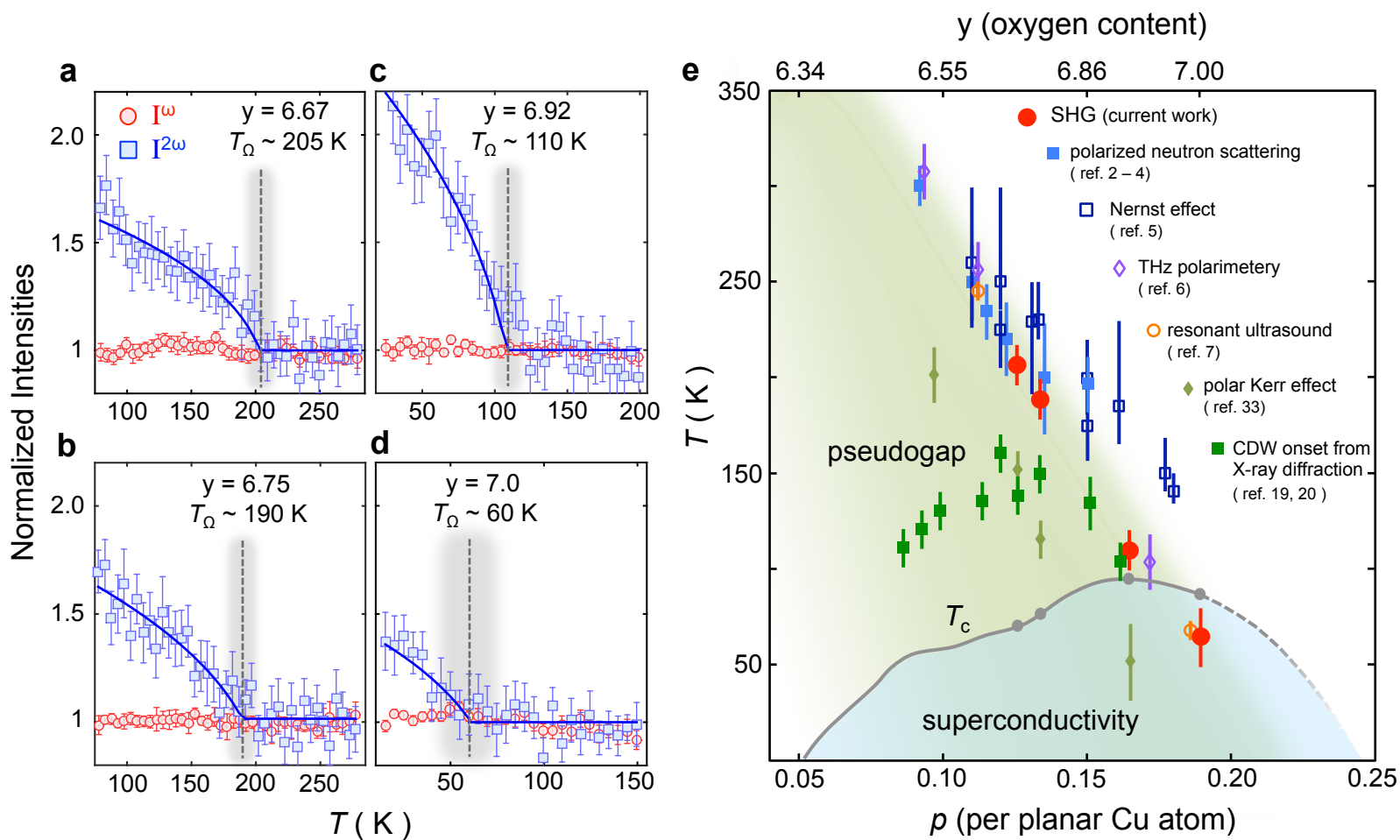


Fig. 3

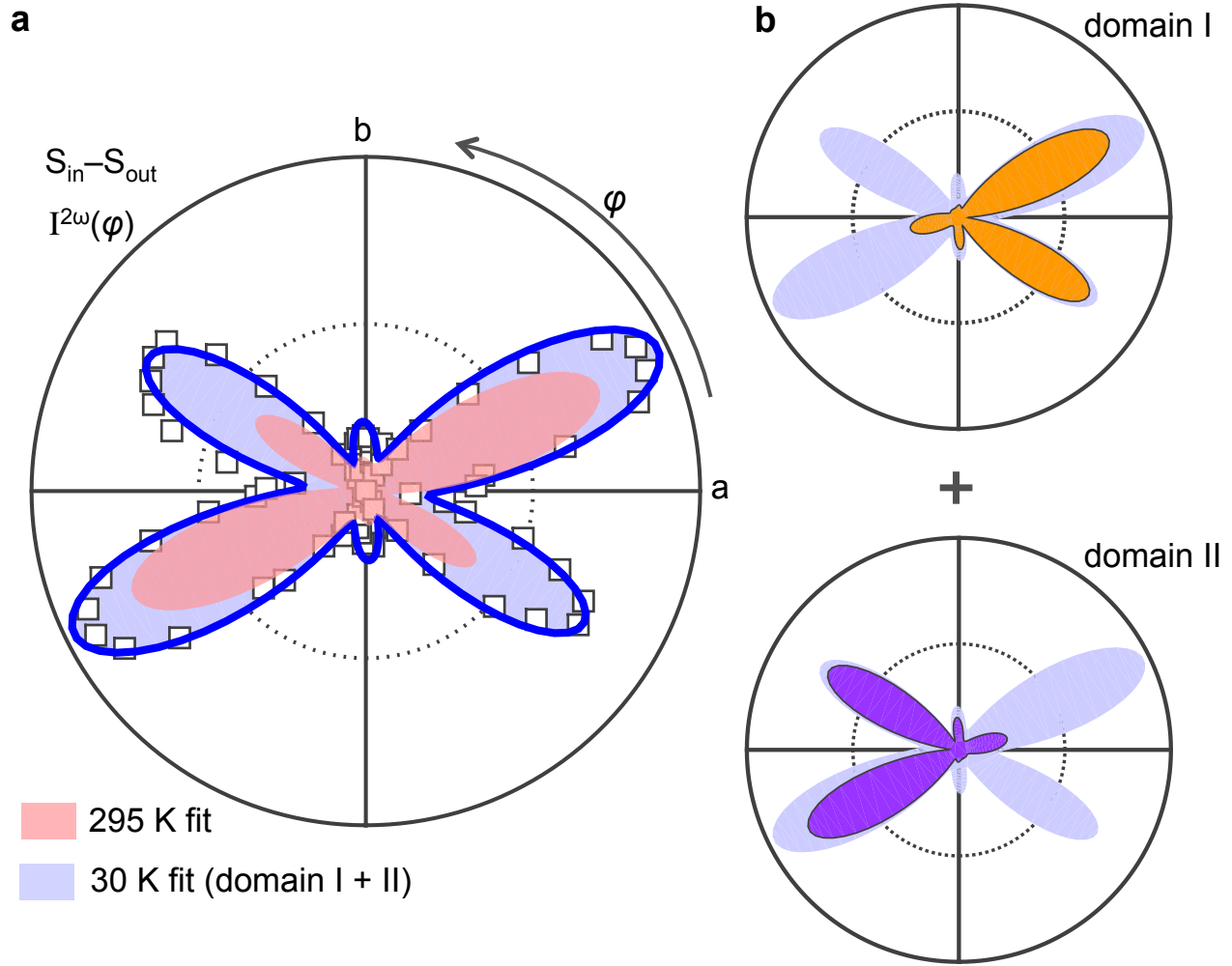


Fig. 4

Supplementary Information for
**A global inversion-symmetry-broken phase inside the pseudogap
region of $\text{YBa}_2\text{Cu}_3\text{O}_y$**

Contents:

- S1. Simulated RA patterns for the orthorhombic mmm point group
- S2. RA data for $P_{\text{in}}-P_{\text{out}}$, $S_{\text{in}}-P_{\text{out}}$ and $P_{\text{in}}-S_{\text{out}}$ geometries above T_{Ω}
- S3. Fits of SH RA data above T_{Ω} to other monoclinic point groups and radiation sources
- S4. Temperature dependence of SH RA data above T_{Ω}
- S5. SH RA patterns above and below T_{Ω} for all doping levels
- S6. List of subgroups of $2/m$
- S7. Exclusion of laser-induced changes to the samples
- S8. Exclusion of misalignment as origin of RA patterns

S1. Simulated RA patterns for the orthorhombic mmm point group

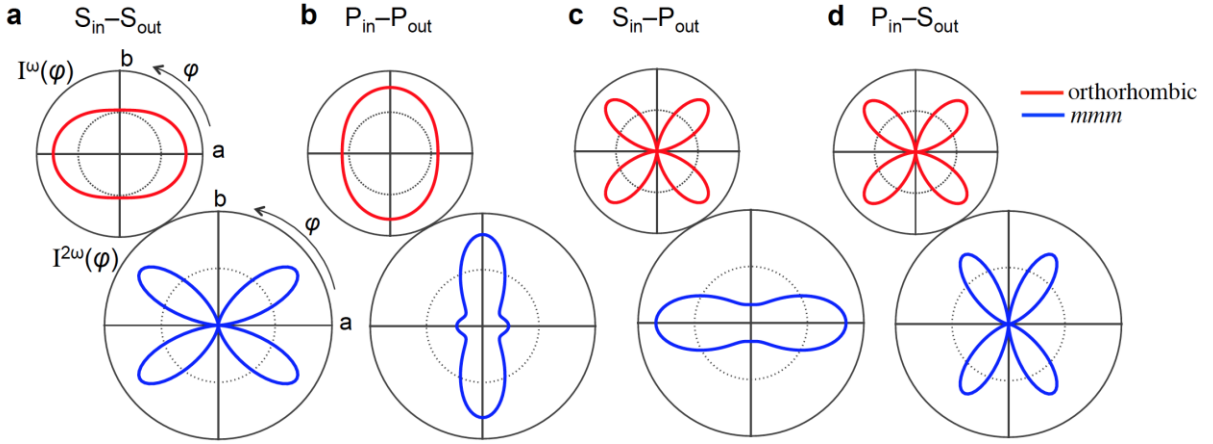


Fig. S1. Simulated linear and SH RA patterns for hole-doped $\text{YBa}_2\text{Cu}_3\text{O}_y$ using an orthorhombic crystal class and mmm point group respectively for all four polarization geometries **a**, $S_{\text{in}}-S_{\text{out}}$ (reproduced from Fig. 1b of the main text), **b**, $P_{\text{in}}-P_{\text{out}}$, **c**, $S_{\text{in}}-P_{\text{out}}$ and **d**, $P_{\text{in}}-S_{\text{out}}$.

We computed linear and SH RA patterns in the electric-dipole and electric-quadrupole approximations for an orthorhombic crystal system and mmm point group respectively. The mathematical expressions for $I^\omega(\varphi)$ and $I^{2\omega}(\varphi)$ are given in the Methods section. In the orthorhombic crystal class χ_{ij}^{ED} has 3 non-zero independent elements (xx , yy , zz). In the mmm point group and degenerate SH configuration χ_{ijkl}^{EQ} has 15 non-zero independent elements ($xxxx$, $xyyy = yyyx$, $xxzz = xzzx$, $xyxy$, $xzxz$, $yxyx = yyxx$, $yxyx$, $yyyy$, $yyzz = yzzy$, $yzyz$, $zxzx$, $zyzy$, $zzxx = zxxz$, $zzyy = zyyz$, $zzzz$). Figure S1 shows the representative RA patterns computed under all four possible polarization geometries. The $P_{\text{in}}-P_{\text{out}}$, $S_{\text{in}}-P_{\text{out}}$ and $P_{\text{in}}-S_{\text{out}}$ simulations reproduce all of the symmetries of the $S_{\text{in}}-S_{\text{out}}$ data shown in Fig. 1b of the main text (Fig. S1a) as expected.

S2. RA data for $P_{in}-P_{out}$, $S_{in}-P_{out}$ and $P_{in}-S_{out}$ geometries above T_{Ω}

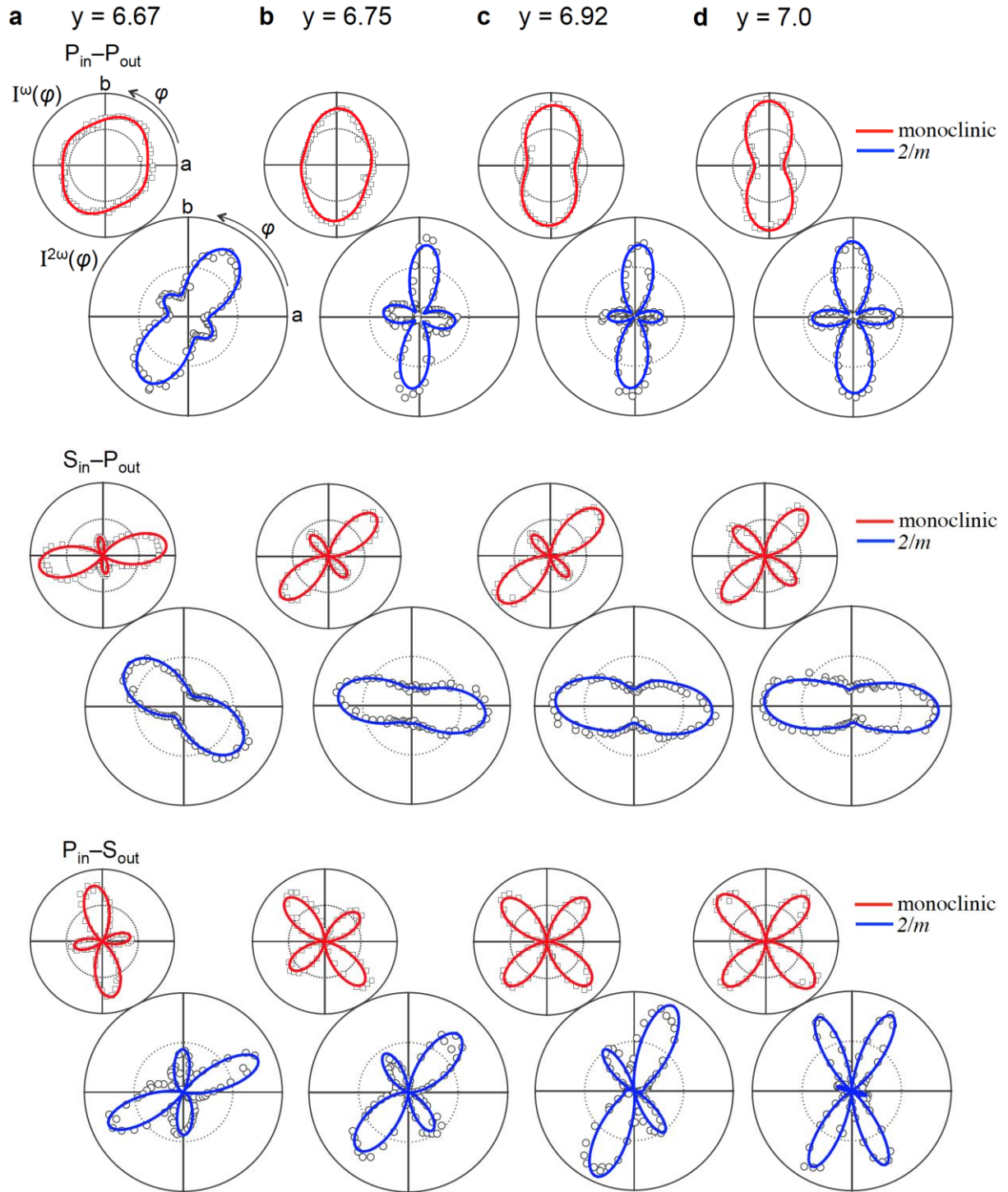


Fig. S2. Linear and SH RA data on hole-doped $YBa_2Cu_3O_y$ with **a**, $y = 6.67$, **b**, $y = 6.75$, **c**, $y = 6.92$ and **d**, $y = 7.0$ in $P_{in}-P_{out}$ (first row), $S_{in}-P_{out}$ (second row), and $P_{in}-S_{out}$ (third row) geometries taken at room temperature. Fits to an electric-dipole induced linear response from a monoclinic crystal system (red curves) and to an electric-quadrupole induced SH response from a $2/m$ point group (blue curves) are overlaid.

Figure S2 shows linear and SH RA data acquired from the four hole-doping levels of $\text{YBa}_2\text{Cu}_3\text{O}_y$ used in this study under $\text{P}_{\text{in}}\text{-P}_{\text{out}}$, $\text{S}_{\text{in}}\text{-P}_{\text{out}}$ and $\text{P}_{\text{in}}\text{-S}_{\text{out}}$ polarization geometries at room temperature. These data violate the symmetries of the orthorhombic crystal class and mmm point group in a manner consistent with the $\text{S}_{\text{in}}\text{-S}_{\text{out}}$ data shown in Fig. 2 of the main text. Using the same mathematical expressions for $I^\omega(\varphi)$ and $I^{2\omega}(\varphi)$ as those used to fit the $\text{S}_{\text{in}}\text{-S}_{\text{out}}$ data shown in Fig. 2 of the main text (see Methods), excellent fits to the data for all doping levels and polarization geometries were obtained (Fig. S2), thus further confirming our monoclinic $2/m$ point group assignment. Figure S2 also shows that the degree of monoclinicity decreases monotonically between $y = 6.67$ and $y = 7$ for all polarization geometries, which corroborates the $\text{S}_{\text{in}}\text{-S}_{\text{out}}$ data shown in Fig. 2 of the main text.

S3. Fits of SH RA data above T_Ω to other monoclinic point groups and radiation sources

i. Electric-dipole induced SH from the 2 point group

By applying C_2 symmetry and the degenerate SH permutation symmetries alone, χ_{ijk}^{ED} is reduced to 8 non-zero independent elements ($xxz = xzx$, $xyx = xzy$, $yxz = yzx$, $yyz = yzy$, zxx , $zxy = zyx$, zyy , zzz), which yields zero response in the S_{in} - S_{out} polarization geometry. By extension, any non-centrosymmetric point group that includes C_2 as a symmetry element cannot generate an electric-dipole induced SH response in S_{in} - S_{out} polarization geometry. Therefore the data shown in Fig. 2 and Fig. 4 of the main text, which have finite S_{in} - S_{out} signals, cannot be explained by any non-centrosymmetric point group that contains C_2 .

ii. Electric-dipole induced SH from the m point group

The m point group explicitly violates C_2 , which is present in all of the room temperature data shown in Fig. 2 of the main text and in Fig. S2. Therefore it is ruled out.

iii. Magnetic-dipole induced SH from the $2/m$ point group

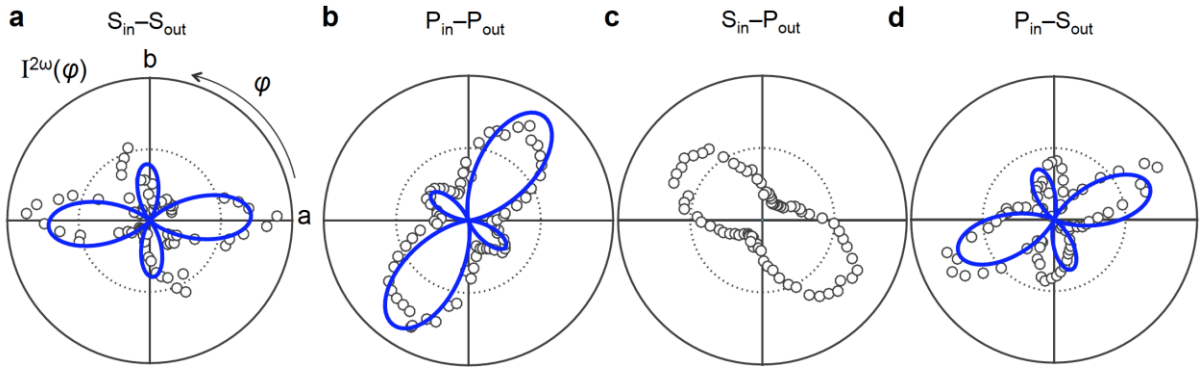


Fig. S3. SH RA data from $YBa_2Cu_3O_{6.67}$ taken in **a**, S_{in} - S_{out} , **b**, P_{in} - P_{out} , **c**, S_{in} - P_{out} , and **d**, P_{in} - S_{out} geometry at room temperature. Blue curves are fits to the bulk magnetic-dipole SH contribution under point group $2/m$.

Magnetic-dipole induced SH is described by the process $M_i^{2\omega} \propto \chi_{ijk}^{MD} E_j^\omega E_k^\omega$ where M is the induced magnetization and E is the incident electric field. The axial rank-3 magnetic-dipole susceptibility tensor χ_{ijk}^{MD} is allowed in centrosymmetric crystals. By applying the $2/m$ point

group symmetries and degenerate SH permutation symmetries, χ_{ijk}^{MD} is reduced to 8 non-zero independent elements ($xxz = xzx$, $xyz = xzy$, $yxz = yzx$, $yyz = yzy$, zxx , $zxy = zy x$, zzy , zzz), which yields zero response in the S_{in} - P_{out} polarization geometry. This clearly disagrees with the data shown in Fig. S2. Moreover, a best fit to other polarization geometries does not provide good agreement (Fig. S3). Therefore the magnetic-dipole response is ruled out.

iv. Surface electric-dipole induced SH from the $2/m$ point group

The surface of any crystal necessarily breaks inversion symmetry and will allow electric-dipole SH generation. However, the (001) surface of a bulk $2/m$ point group contains C_2 and therefore yields zero response in S_{in} - S_{out} polarization geometry based on the arguments presented in sub-section (i). Therefore the SH response observed above T_Ω must originate from a source other than the surface electric-dipole contribution.

We note that the additional SH intensity observed below T_Ω (Figs 3 & 4 of main text) also cannot originate from the surface. First, the temperature at which this symmetry breaking occurs coincides with the known bulk T^* value for all different doping levels studied. Second, if the enhancement of SH intensity observed below T^* did in fact originate from the surface, it would imply a corresponding enhancement of the surface electric-dipole radiation efficiency at 1.5 eV incident energy. However the bulk sensitive linear optical response, which is likewise sensitive to electric-dipole transitions at 1.5 eV, shows no detectable change across T^* (Fig. 3 main text). The only way to reconcile these statements is if a significant change in electric-dipole transition rates at 1.5 eV happened to take place exclusively at the surface across the bulk T^* value, which to our knowledge has no experimental or theoretical precedent. Therefore we rule out this scenario.

S4. Temperature dependence of SH RA data above T_{Ω}

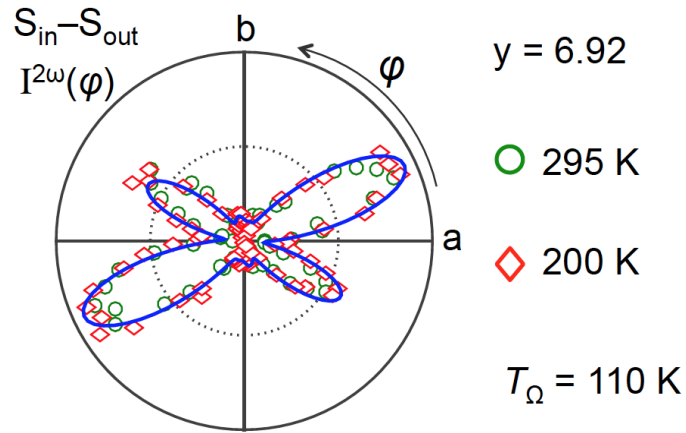


Fig. S4. SH RA data from $\text{YBa}_2\text{Cu}_3\text{O}_{6.92}$ acquired in $S_{\text{in}}-S_{\text{out}}$ polarization geometry at temperatures $T = 295 \text{ K}$ (green circles) and $T = 200 \text{ K}$ (red diamonds), which are both well above $T_{\Omega} \sim 110 \text{ K}$. The blue curve is a best fit to the $T = 295 \text{ K}$ data assuming electric-quadrupole induced SH from a $2/m$ point group.

To search for changes in crystallographic structure at temperatures above T_{Ω} , we performed SH RA measurements as a function of temperature for $T > T_{\Omega}$. No changes in both intensity and pattern shape were detected above T_{Ω} across all four doping levels and polarization geometries. Figure S4 shows representative SH RA patterns from $\text{YBa}_2\text{Cu}_3\text{O}_{6.92}$ in $S_{\text{in}}-S_{\text{out}}$ geometry acquired at $T = 200 \text{ K}$ and $T = 295 \text{ K}$, which are both well above its measured value of $T_{\Omega} \sim 110 \text{ K}$ and are nearly identical. This shows that the monoclinic distortion of the lattice sets in above room temperature.

S5. SH RA patterns above and below T_{Ω} for all doping levels

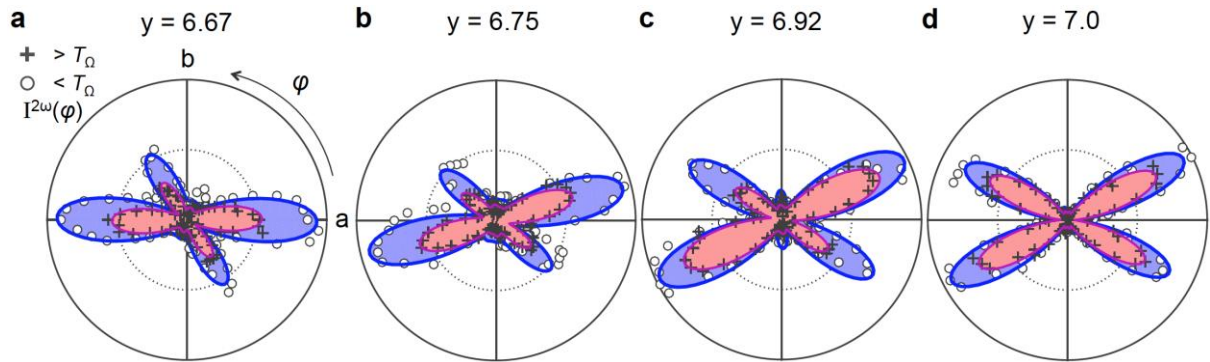


Fig. S5. SH RA data from hole-doped $\text{YBa}_2\text{Cu}_3\text{O}_y$ taken in $S_{\text{in}}-S_{\text{out}}$ polarization geometry both above (crosses) and below (circles) T_{Ω} . The high temperature data were all acquired at $T = 295$ K while the low temperature data were acquired at **a**, $T = 80$ K for $y = 6.67$, **b**, $T = 80$ K for $y = 6.75$, **c**, $T = 30$ K for $y = 6.92$ and **d**, $T = 15$ K for $y = 7.0$. Red and blue shaded regions are the best fits to the high and low temperature data respectively using the same models as those described in Fig. 4 of the main text.

Figure S5 shows the SH RA patterns taken both above and below T_{Ω} for the complete set of doping levels in $S_{\text{in}}-S_{\text{out}}$ polarization geometry. For all doping levels, the intensity is enhanced below T_{Ω} consistent with Fig. 3 of the main text and fit excellently to the same two domain model applied to the data shown in Fig. 4 of the main text.

S6. List of subgroups of $2/m$

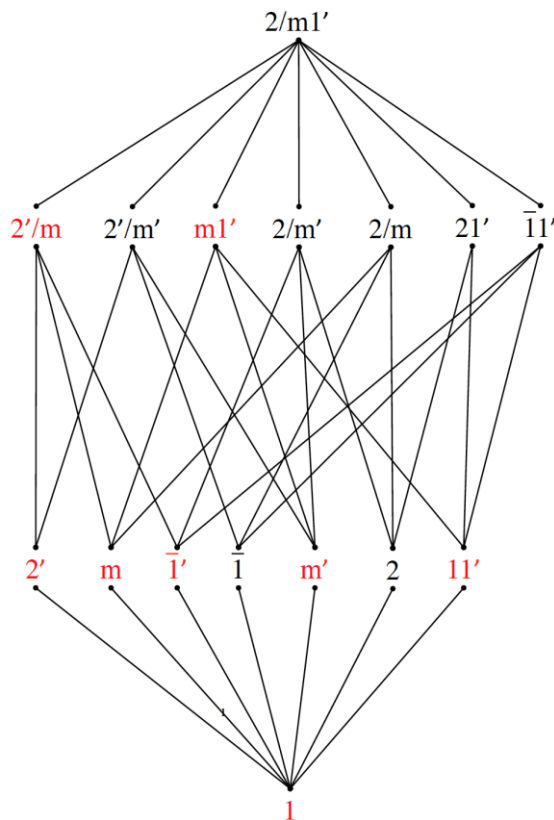


Fig. S6. Tree diagram showing all magnetic and non-magnetic subgroups of the $2/m$ point group (re-written as $2/m1'$). Lines connect parent groups to their subgroups. The non-centrosymmetric subgroups that do not contain C_2 are shown in red.

The complete set of magnetic and non-magnetic subgroups of the crystallographic monoclinic point group $2/m$ is displayed in Fig. S6. The point group $2/m$ is re-written as $2/m1'$ to make the relationship to its magnetic subgroups more obvious. The generators are defined as follows: $2 \rightarrow 180^\circ$ rotation about the c -axis, $m \rightarrow$ reflection about ab -plane, $1 \rightarrow$ identity, $\bar{1} \rightarrow$ spatial inversion, $A' \rightarrow$ combination of any spatial operation A with time-reversal. There are a total of 15 subgroups of $2/m1'$ (excluding $2/m1'$ itself) of which the 8 shown in red are non-centrosymmetric and do not contain C_2 . The $2'/m$ and $m1'$ subgroups are independent (i.e. one is not a subgroup of the other) and contain all of the other 6 red subgroups.

S7. Exclusion of laser-induced changes to the samples

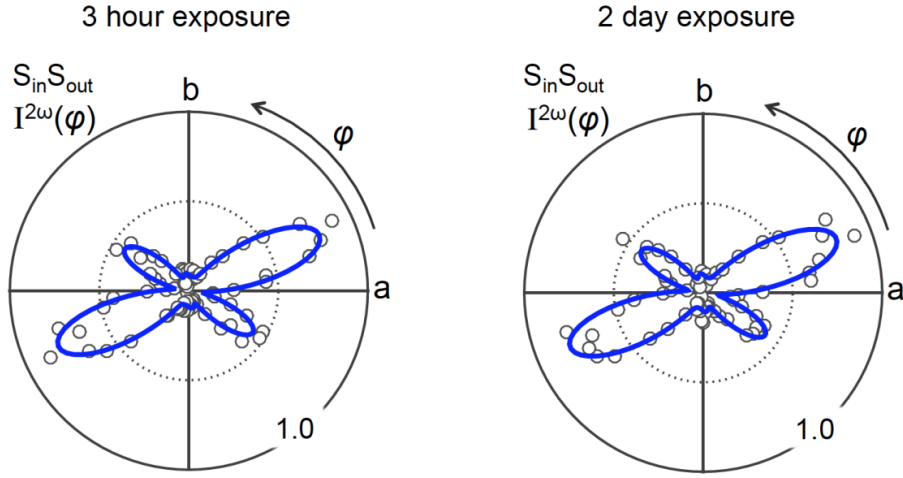


Fig. S7. SH RA data from optimal doped $\text{YBa}_2\text{Cu}_3\text{O}_{6.92}$ taken in $S_{\text{in}}\text{-}S_{\text{out}}$ polarization geometry at $T = 295$ K following a 3 hour and 2 day exposure to laser light. Blue curves are fits as described in the main text.

To verify that the laser beam is not inducing any change in the samples, particularly not creating additional oxygen vacancies, we performed SH RA measurements following different laser exposure times. Knowing that the SH RA patterns are highly sensitive to oxygen content (Fig. 2 main text), if the laser were inducing additional oxygen vacancies, one would expect the SH RA patterns to evolve towards those associated with lower oxygen content upon increased laser exposure time. However, we do not observe any obvious change in the SH RA pattern as a function of continuous laser exposure time for any of the samples studied. To give an example, Fig. S7 shows a comparison of two room temperature SH RA patterns measured from the same spot on an optimal doped sample ($y = 6.92$) after 3 hours versus 2 days of laser exposure plotted on the same intensity scale, which show no measurable difference. [Note: 3 hours is the typical time we require to align the sample]. Moreover, for all doping levels studied, the onset temperatures T_{Ω} of the symmetry breaking coincide with the known values of T^* (Fig. 3e main text). Therefore, we rule out any laser-induced changes to the samples.

S8. Exclusion of misalignment as origin of RA patterns

We can rule out misalignment of any form as the origin of the observed RA patterns for the following independent set of reasons:

1) The flat as-grown faces of the crystals are extremely well aligned perpendicular to the c -axis. We know this because atomic force microscopy performed on as-grown crystals show very large micron sized terraces separated by unit-cell tall steps. Therefore any angular misalignment between the surface normal and the c -axis would not exceed approximately $1 \text{ nm (step height)} / 1000 \text{ nm (terrace length)} = 0.001 \text{ radians} \approx 0.06^\circ$.

The experimental optical axis is also extremely well aligned perpendicular to the crystal surface. This alignment is performed by ensuring overlap between a collimated incident beam and the retro-reflected beam over a distance of 1 m. Therefore any angular misalignment between the optical axis and the surface normal would not exceed approximately $1 \text{ mm (collimated beam diameter)} / 1000 \text{ mm (beam overlap distance)} = 0.001 \text{ radians} \approx 0.06^\circ$.

The two facts above together demonstrate that the experimental optical axis is extremely well aligned to the crystallographic c -axis.

2) The observed deviation from mmm symmetry exhibits a systematic dependence on doping (Fig. 2 main text), which is unlikely to arise from random misalignment especially given that the identical alignment procedure is used for all samples.

3) A crystal with mmm point group symmetry only has three axes of two-fold rotational symmetry, namely the orthorhombic a -, b - and c -axes. Therefore if the optical axis of the experiment is not along one of these axes, the RA patterns will not exhibit two-fold rotational symmetry. The fact that we do observe two-fold rotational symmetry in the RA patterns (Fig. 2 main text) thus excludes the possibility that what we observe results simply from a small c -axis misalignment of an orthorhombic crystal.